



Technical Notes

Liver vessel segmentation based on extreme learning machine

Ye Zhan Zeng^a, Yu Qian Zhao^{a,b,*}, Miao Liao^a, Bei Ji Zou^b, Xiao Fang Wang^c, Wei Wang^d^a Department of Biomedical and Information Engineering, Central South University, Changsha 410083, China^b School of Information Science and Engineering, Central South University, Changsha 410083, China^c Department of Mathematics and Computer Science, École centrale de Lyon, Écully, France^d The Third Xiangya Hospital of Central South University, Changsha 410083, China

ARTICLE INFO

Article history:

Received 12 November 2015

Received in Revised form 6 February 2016

Accepted 8 April 2016

Available online 4 May 2016

Keywords:

Segmentation

Liver vessels

CT

ELM

ABSTRACT

Liver-vessel segmentation plays an important role in vessel structure analysis for liver surgical planning. This paper presents a liver-vessel segmentation method based on extreme learning machine (ELM). Firstly, an anisotropic filter is used to remove noise while preserving vessel boundaries from the original computer tomography (CT) images. Then, based on the knowledge of prior shapes and geometrical structures, three classical vessel filters including Sato, Frangi and offset medialness filters together with the strain energy filter are used to extract vessel structure features. Finally, the ELM is applied to segment liver vessels from background voxels. Experimental results show that the proposed method can effectively segment liver vessels from abdominal CT images, and achieves good accuracy, sensitivity and specificity.

© 2016 Associazione Italiana di Fisica Medica Published by Elsevier Ltd. All rights reserved.

Introduction

Liver-vessel segmentation from computer tomography (CT) images is critical to computer-aided diagnosis and hepatic disease treatment [1]. For example, the analysis of hepatic vessel morphology and branching pattern is a requisite step in liver surgery operation. Due to the significant noise and complex inhomogeneous background, accurate vessel segmentation from liver images is a challenging task, especially for highly branched vessel system. Generally, the accurate vessel segmentation is performed manually by the doctors through delineating vessel contours on each slice. However, manual segmentation of those vessels is extremely tedious and highly dependent on the operator's experience and skill, and therefore, automatic liver-vessel segmentation has attracted increasing research attention.

A variety of approaches have been developed for 3D vessel detection and segmentation [2]. Usually, 3D vessels in medical images are considered as tubular structures with a radial symmetry cross-section, and based on this shape characteristic, many filters had been devised for vessel detection. For example, Frangi et al. [3] developed a multi-scale tubular filter for 2D/3D vessel detection according to the eigenvalues of a Hessian matrix. Xiao et al. [4] presented a bi-Gaussian filter for adjacent curvilinear

structure detection by the integration of traditional Gaussian and rectangle kernels. The flux-based filter is often applied to deal with the closely adjacent objects like parallel or intertwined vessels [5]. Law and Chung [6] developed an optimally oriented flux (OOF) filter to delineate tubular structures, and utilized a Fast Fourier Transform (FFT) algorithm to reduce computation cost. Considering the multiple directions of image gradient flux, Turetken et al. [7] devised a multi-directional oriented flux (MDOF) method by finding multiple directions and radii of maximal response of the joint oriented flux and anti-symmetry operators.

For vessel segmentation, Lorigo et al. [8] constructed a CURVES system by modeling vessels as 3D curves with arbitrary branching, and employed an active contour model to segment these curves from magnetic resonance angiography (MRA) and CT images. Shang et al. [9] utilized a region competition-based active contour combined with Gaussian mixture model to segment thick vessels, and defined a vascular vector field to drive the active contour into thin and weak vessels. Bauer et al. [10] proposed a method for the segmentation of interwoven 3D tubular tree structures based on shape priors and graph cuts, and their method was verified to be robust against disturbance induced by interwoven vessel systems. Esneault et al. [11] introduced a liver-vessel segmentation method based on hybrid geometrical moments and graph cuts, in which a 3D geometrical moment-based detector of cylindrical shapes together with graph cuts was used to extract liver vessels. Hemmati et al. [12] first applied a mean shift filter to increase the uniformity of vessels, followed by a fast marching algorithm

* Corresponding author at: Department of Biomedical and Information Engineering, Central South University, Changsha 410083, China.

E-mail addresses: zyq@csu.edu.cn (Y.Q. Zhao), cjr.wangwei@vip.163.com (W. Wang).

to extract the centerlines, and finally used a 3D level set method for carotid-lumen segmentation. Conversano et al. [13] proposed a hepatic vessel segmentation method or 3D planning for liver surgery, in which the Frangi filter is used to enhance vessel structures and an experimental segmentation threshold is applied for vessel segmentation.

Due to the complexity of 3D liver-vessel images, few studies have been published for liver-vessel segmentation. In this paper, we present a novel method for liver-vessel segmentation from contrast-enhanced CT images based on extreme learning machine (ELM). First, an anisotropic filter is used to suppress noise and simultaneously keep boundary details, and then, based on the shape priors of vessel structures, four filters including Sato, Frangi, offset medialness and strain energy filters are applied to extract vessel features. Finally, an ELM is applied to train and recognize liver vessels from background.

The proposed method aims at applying the machine learning method for liver-vessel segmentation. To improve the efficiency of the proposed method, the ELM is considered due to its fast learning speed. The hidden-node number of the ELM is selected by balancing the training time and segmentation sensitivity. Compared with previous works, the ELM does not require manual selection of the initial vessel seeds for each CT volume as the traditional GAC and region growing methods do, and it involves only few parameters which can be easily confirmed in a reasonable range. Moreover, since the four filters work well for the detection of general tubular structures, our method can be generalized for other 3D vessel extraction like cerebral vascular vessels.

The rest of this paper is organized as follows. The details of the proposed method for liver-vessel segmentation are described in Section “Methodology”. Section “Experiments” presents the evaluations and comparisons of experimental results, and the conclusions are drawn in Section “Discussion and conclusions”.

Methodology

Preprocessing

The 3D liver images were obtained from a serial of abdominal CT slices with their corresponding binary liver masks, as shown in Fig. 1(a). Since liver vessels in these liver images suffer from significant noise and low contrast, they are first enhanced by adjusting window width/level (see Fig. 1(b)), and then smoothed by a nonlinear anisotropic diffusion filter to minimize the impact of inhomogeneous background. The anisotropic diffusion filter is defined as:

$$\begin{cases} I_t(x, y, z, t) = \text{div}(c(x, y, z, t) \nabla I) \\ I_t(x, y, z, 0) = I_0(x, y, z) \end{cases} \quad (1)$$

where $I_t(x, y, z, t)$ denotes the image at time t , $I_0(x, y, z)$ the original image, div the divergence operator, and ∇I the gradient of image I . The conduction coefficient $c(x, y, z, t)$ represents a nonnegative monotonically decreasing function, which is defined as:

$$c(x, y, z, t) = e^{-(\|\nabla I\|/d)^2} \quad (2)$$

where d is a gradient modulus threshold, and is set as 70 in this paper. Figure 1(c) shows an example of anisotropic diffusion filtering for Fig. 1(b), from which we can find that the noise is filtered effectively and the vessel edges are preserved well.

Vessel feature extraction

In this paper, the combination of Sato, Frangi, offset medialness and strain energy filters is used to extract vessel features for ELM training and testing based on the knowledge of prior shape and geometrical structure. The Sato and Frangi filters are used to detect 3D vessel structures, the offset medialness filter to extract vessel topologies, and the strain energy filter to enhance complex structures like bifurcations and branches. All these filters are based on a Hessian matrix which is usually introduced to describe vessel structure based on the distribution of eigenvalues. For a three-dimensional image, the scale-space Hessian matrix is a 3×3 matrix defined as:

$$H_{\sigma(x,y,z)} = \sigma^2 \begin{bmatrix} \frac{\partial^2 I_{\sigma(x,y,z)}}{\partial x^2} & \frac{\partial^2 I_{\sigma(x,y,z)}}{\partial x \partial y} & \frac{\partial^2 I_{\sigma(x,y,z)}}{\partial x \partial z} \\ \frac{\partial^2 I_{\sigma(x,y,z)}}{\partial y \partial x} & \frac{\partial^2 I_{\sigma(x,y,z)}}{\partial y^2} & \frac{\partial^2 I_{\sigma(x,y,z)}}{\partial y \partial z} \\ \frac{\partial^2 I_{\sigma(x,y,z)}}{\partial z \partial x} & \frac{\partial^2 I_{\sigma(x,y,z)}}{\partial z \partial y} & \frac{\partial^2 I_{\sigma(x,y,z)}}{\partial z^2} \end{bmatrix} \quad (3)$$

where I_{σ} is a Gaussian smoothed image at scale σ . Let λ_1 , λ_2 , and λ_3 equal the eigenvalues of $H_{\sigma(x,y,z)}$ satisfying $|\lambda_1| \geq |\lambda_2| \geq |\lambda_3|$; a bright vessel structure will have $\lambda_1 \approx \lambda_2 \leq 0$ with their eigenvectors v_1 and v_2 defining a cross-section plane, and $\lambda_3 \approx 0$ with its eigenvector v_3 corresponding to the vessel tangent direction, as shown in Fig. 2.

Sato filter

The Sato filter is a standard Insight Segmentation and Registration Toolkit (ITK) filter [14], which is defined as:

$$f = \begin{cases} \lambda_c \cdot \exp\left(-\frac{\lambda_3^2}{2(\alpha_1 \lambda_c)^2}\right) & \lambda_3 \leq 0, \lambda_c \neq 0 \\ \lambda_c \cdot \exp\left(-\frac{\lambda_3^2}{2(\alpha_2 \lambda_c)^2}\right) & \lambda_3 > 0, \lambda_c \neq 0 \\ 0 & \lambda_c = 0 \end{cases} \quad (4)$$

where $\lambda_c = \min(-\lambda_2, -\lambda_1)$, α_1 and α_2 are penalty coefficients based on the sign of λ_3 to weaken the response of blob-like structure such

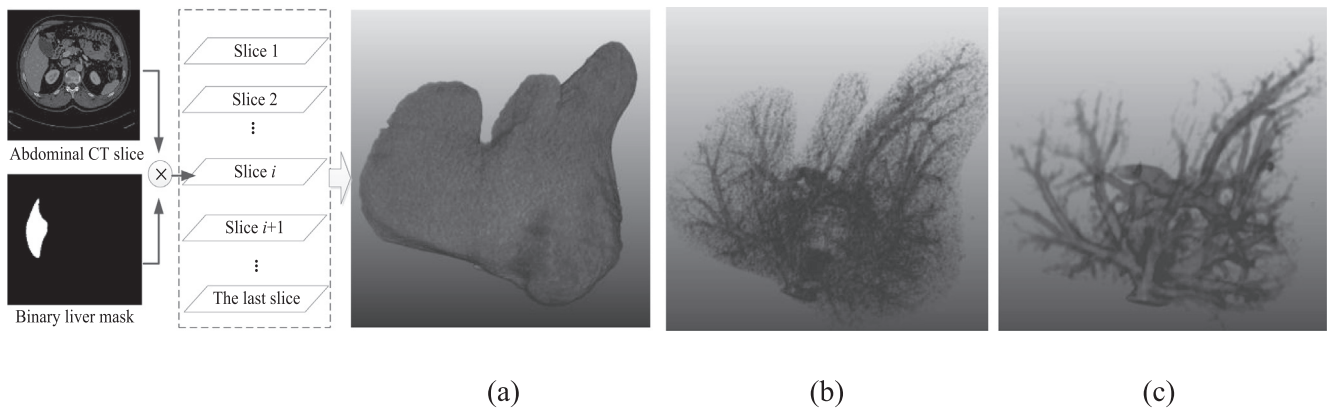


Figure 1. Example of preprocessing. (a) Original liver image, (b) result of adjusting window width/level, and (c) result of anisotropic diffusion filtering.

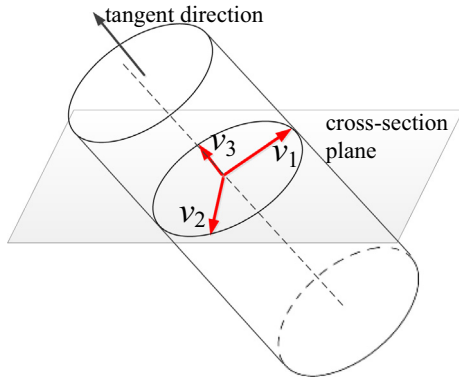


Figure 2. 3D vessel model and its corresponding eigenvectors. Orthogonal vectors v_1 and v_2 define an cross-section plane, and v_3 represents the vessel tangent direction.

as the noise and are set as 0.5 and 2.0 in this paper, respectively. To account for the variety of vessel sizes, a multi-scale Sato filter is obtained by calculating the maximum response of the single-scale filters:

$$\varphi_{\text{sato}}(\bar{x}) = \max\{f(\sigma, \bar{x}), \sigma_{\min} < \sigma < \sigma_{\max}\} \quad (5)$$

where $\bar{x} = (x, y, z)$, σ_{\min} , and σ_{\max} are minimum and maximum radii and are set as 0.5 and 8.5, respectively. Figure 3(a) shows the Sato filtering result of Fig. 1(c).

Frangi filter

Due to the intuitive geometric formulation, the Frangi filter was frequently used to discriminate tubular-like structures, and is defined as:

$$V_F = \begin{cases} 0, & \text{if } \lambda_1 \geq 0 \text{ or } \lambda_2 \geq 0 \\ \left(1 - \exp\left(-\frac{R_A^2}{2\sigma_F^2}\right)\right) \exp\left(-\frac{R_B^2}{2\beta_F^2}\right) \left(1 - \exp\left(-\frac{S^2}{2C_F^2}\right)\right), & \text{other} \end{cases} \quad (6)$$

where $R_B = |\lambda_3|/\sqrt{|\lambda_1\lambda_2|}$ is the geometric ratio based on the second order ellipsoid and accounts for the deviation from a blob-like structure, $R_A = |\lambda_2|/|\lambda_1|$ is used to distinguish the plate- and line-like structures, $S = \sqrt{\sum_{j=1}^3 \lambda_j^2}$ represents the noise control parameter, and α_F , β_F , and C_F are thresholds controlling the filter sensitivity to the measures R_A , R_B , and S , respectively, and are experientially set as 0.5, 0.5, 20 in this paper. The multi-scale Frangi filter $\varphi_{\text{frangi}}(\bar{x})$ is given by:

$$\varphi_{\text{frangi}}(\bar{x}) = \max\{V_F(\sigma, \bar{x}), \sigma_{\min} < \sigma < \sigma_{\max}\} \quad (7)$$

Figure 3(b) shows the Frangi filtering result of Fig. 1(c), from which it is apparent that the Frangi filter is more effective in suppressing noise and background than the Sato filter.

Offset medialness filter

The offset medialness filter was first introduced for 3D vessel detection by Krissian et al. [15], which depends on the Hessian to find tangent directions and the boundary gradient to estimate local radii. The initial offset medialness filter measures tube-likeness by calculating the average gradient projections taken in radial directions around a circle in the cross-section plane given by the eigenvectors v_1 and v_2 , and is defined as

$$\bar{b}_{\sigma_b}(\bar{x}, r) = \frac{1}{N_c} \sum_{i=0}^{N_c-1} \sigma_b |\nabla I_{\sigma_b}(\bar{x} + r v_{\alpha_i}) v_{\alpha_i}|, \quad \text{with } \alpha = 2\pi i/N_c \quad (8)$$

where N_c represents the number of samples calculated by $N_c = \lfloor 2\pi r + 1 \rfloor$, r the circle radius, v_{α} the radial direction denoted as $v_{\alpha} = v_1 \cos \alpha + v_2 \sin \alpha$, and ∇I_{σ_b} the gradient vector of I_{σ_b} with $\sigma_b = r^\eta$ ($0 \leq \eta \leq 1$), where η is the scale-normalizing coefficient to balance boundary shape constraint and noise suppression and is set as 0.7 in this paper. However, Eq. (8) also produces response for isolated edges and non-tube-like structures due to their high intensity variation, to avoid which a circular symmetry property is taken into account. For an ideal vessel cross-section shown in Fig. 4, the gradient directions at the vessel boundary all point directly towards the center, and the corresponding gradient amplitudes are equal. To describe this symmetry property, we define the i th boundary sample by

$$b_i = \sigma_b |\nabla I_{\sigma_b}(\bar{x} + r v_{\alpha_i}) v_{\alpha_i}| \quad (9)$$

whose variance can be calculated by

$$s^2(\bar{x}, r) = \frac{1}{N_c} \sum_{i=0}^{N_c-1} (b_i - \bar{b})^2 \quad (10)$$

In fact, for a circular symmetric cross-section or a smaller deviation from a standard circular cross-section, the variance s^2 is low, while for an asymmetric cross-section, s^2 is very high. Therefore, a symmetry function based on s^2 is introduced and is denoted as:

$$\tau(\bar{x}, r) = 1 - \frac{s^2(\bar{x}, r)}{\bar{b}^2} \quad (11)$$

Obviously, the value of τ with a radial symmetric cross-section is larger than that with a non-symmetric one. Thus, the final offset medialness at radius r is defined as:

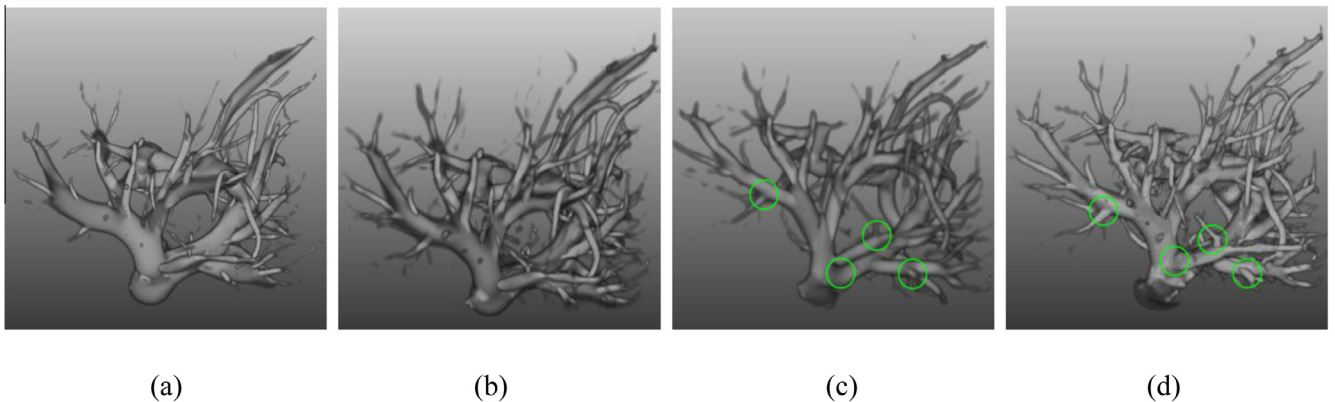


Figure 3. Filtering results of (a) Sato, (b) Frangi, (c) offset medialness, and (d) strain energy filters for Fig. 1(c), respectively.

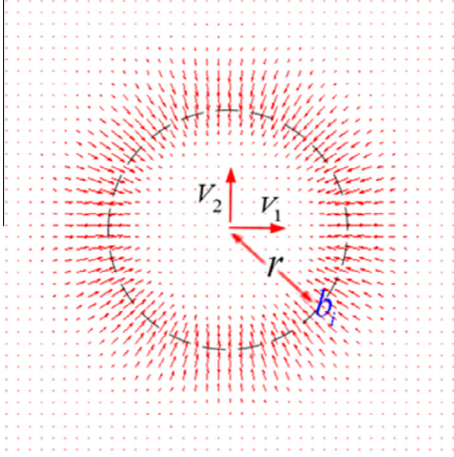


Figure 4. The gradient distribution of an ideal vessel cross-section. The length and direction of arrows represent the gradient's magnitude and direction, respectively.

$$M(\bar{x}) = \begin{cases} 0, & \text{if } \lambda_1 > 0 \text{ or } \lambda_2 > 0 \\ b \cdot \tau(\bar{x}, r), & \text{else.} \end{cases} \quad (12)$$

To obtain the optimal response over different radii, a traditional multi-scale framework is utilized for offset medialness filter, which is given by

$$\phi_{\text{medial}}(\bar{x}) = \max\{M(r, \bar{x}), r_{\min} < r < r_{\max}\} \quad (13)$$

where r_{\min} and r_{\max} represent the minimum and maximum radii and are set as 0.5 and 8.5, respectively, to make them consistent with σ_{\min} and σ_{\max} . The offset medialness filtering result of Fig. 1 (c) is shown in Fig. 3(c).

Strain energy filter

The strain energy filter was motivated by the achievement of stress-strain principles in mechanics, and was applied for 3D vessel enhancement in pulmonary CT and fMRI images [16]. In this paper, we utilize this filter to preserve vascular structures like the bifurcations and branches.

According to stress and strain theory, the stress tensor can be considered as a Hessian matrix, and can be decomposed as

$$H = \bar{H} + \tilde{H} \quad (14)$$

where \bar{H} is the isotropic or spherical component representing the mean stress in varying orientations, \tilde{H} represents the anisotropic component showing the directional inequality information of stress. \bar{H} and \tilde{H} are respectively calculated by

$$\bar{H} = \frac{1}{3} \text{tr}(H) \mathbf{I} = \frac{1}{3} (H : \mathbf{I}) \mathbf{I} \quad (15)$$

$$\tilde{H} = H - \frac{1}{3} \text{tr}(H) \mathbf{I} = H - \frac{1}{3} (H : \mathbf{I}) \mathbf{I} \quad (16)$$

where $\text{tr}(\cdot)$ is the trace operator and \mathbf{I} is a unit matrix.

Based on the link between image structures and local loading states of material, in strain energy filter, a strain energy density is introduced for a measure of structure strength, and a shape discrimination function is devised from the orthogonal tensor decomposition. The strain energy density is defined as:

$$\rho = \sqrt{(1-2\nu)(\bar{H} : \bar{H}) + (1+\nu)(\tilde{H} : \tilde{H})} \quad (17)$$

where ν is the Poisson ratio. Note that if $\nu < 0$, the intensity concentrating on one direction will lead to a relative intensity increasing in

the perpendicular directions, which is known to generate isotropic “blob” structures. On the contrary, if $\nu > 0$, it will cause the opposite result in orthogonal directions. Owing to the importance of preserving vessel connectivity at bifurcations, ν is preferred to be a positive value and is set as 0.2 in this paper.

By investigating the general vessel shape, the shape discrimination function is given by

$$V_s(\bar{x}) = \begin{cases} \sqrt{FA}, & \text{if } FA < 1 \\ \frac{1}{2}(\text{mode}(\bar{x}) + 1), & \text{otherwise} \end{cases} \quad (18)$$

where FA is a fractional anisotropy and $\text{mode}(\bar{x})$ is the skewness of eigenvalues, and they can be defined as:

$$FA = \sqrt{\frac{(\lambda_1 - \lambda_2)^2 + (\lambda_1 - \lambda_3)^2 + (\lambda_2 - \lambda_3)^2}{\lambda_1^2 + \lambda_2^2 + \lambda_3^2}} \quad (19)$$

$$\text{mode}(\bar{x}) = \sqrt{2} \frac{\frac{1}{3} \sum_{i=1}^3 (\lambda_i - \bar{\lambda})^3}{\left(\frac{1}{3} \sum_{i=1}^3 (\lambda_i - \bar{\lambda})^2\right)^{\frac{3}{2}}} \quad (20)$$

where $\bar{\lambda}$ is the average eigenvalue. The final weighted strain energy filter is defined:

$$\phi(\sigma, \bar{x}) = \begin{cases} 0, & \text{if } \frac{1}{3}(\lambda_1 + \lambda_2 + \lambda_3) > -\alpha_s \lambda_m \\ \exp\left(-\theta_s \frac{\|\nabla I\|}{\lambda_m}\right) V_s^\kappa(\bar{x}) \rho(H, \nu), & \text{else.} \end{cases} \quad (21)$$

where λ_m is the maximum magnitude of eigenvalues, α_s is adopted to adjust sensitivity to ensure noise immunity, $\exp\left(-\theta_s \frac{\|\nabla I\|}{\lambda_m}\right)$ is used to suppress step-edges and to prevent small object from being overlapped by larger smoothing kernels, and θ_s and κ are respectively applied to adjust the sensitivity of the filter response and the sharpness of shape selectivity. In this paper, the parameters α_s , θ_s and κ are set as 0.1, 0.02, and 0.5, respectively. By repetitive computation for different radii, the multi-scale strain energy filter ϕ_{strain} is computed as:

$$\phi_{\text{strain}}(\bar{x}) = \max\{\phi(\sigma, \bar{x}), \sigma_{\min} < \sigma < \sigma_{\max}\} \quad (22)$$

Figure 3(d) gives an example for strain energy filtering, from which it can be found that this filter shows a better performance on enhancement for vessel branches and bifurcations than the medialness filter.

ELM training and classification

The ELM was originally presented by Huang et.al [17] for the single-hidden layer feed forward neural networks, and was then extended to the generalized single-hidden layer feed forward networks (SLFNs). Since the hidden nodes of ELM are randomly initiated and fixed without iteratively learning, and therefore, it provides a better performance on training speed than the traditional machine learning method like Support Vector Machine (SVM).

For N training samples, the output of SLFNs with L hidden nodes, whose network structure is shown in Fig. 5, can be denoted as:

$$f_L(\bar{x}) = \sum_{i=1}^L \beta_i h_i(\bar{x}) = \mathbf{h}(\bar{x}) \beta \quad (23)$$

where $\beta = [\beta_1, \dots, \beta_L]^T$ represents output weights connecting the hidden nodes and the output nodes, $\mathbf{h}(\bar{x}) = [h_1(\bar{x}), \dots, h_L(\bar{x})]$ the output vector of the hidden layer with respect to input \bar{x} . Eq. (23) can be written compactly as $\mathbf{H}_E \beta = \mathbf{T}$ with

$$\mathbf{H}_E = \begin{bmatrix} \mathbf{h}(\bar{x}_1) \\ \vdots \\ \mathbf{h}(\bar{x}_N) \end{bmatrix} = \begin{bmatrix} h_1(\bar{x}_1) & \cdots & h_L(\bar{x}_1) \\ \vdots & \vdots & \vdots \\ h_1(\bar{x}_N) & \cdots & h_L(\bar{x}_N) \end{bmatrix} \quad (24)$$

where \mathbf{T} is the training data target matrix and \mathbf{H}_E the hidden layer output matrix of the SLFNs.

According to Eqs. (23) and (24), the output weights β can be obtained using Moore–Penrose generalized inverse $\hat{\mathbf{H}}_E^+$:

$$\beta = \hat{\mathbf{H}}_E^+ \mathbf{T} = \begin{cases} \mathbf{H}_E^T (\frac{1}{c} + \mathbf{H}_E \mathbf{H}_E^T)^{-1} \mathbf{T} & \text{when } N < L \\ (\frac{1}{c} + \mathbf{H}_E^T \mathbf{H}_E)^{-1} \mathbf{H}_E^T \mathbf{T} & \text{when } L < N \end{cases} \quad (25)$$

where positive value $1/c$ is added for better generalization performance.

To reduce the classification error caused by different intensity ranges of the four vessel features obtained from the aforementioned four filters, we normalize each feature (i.e., vessel filtering result) by

$$\hat{\varphi}_i = \frac{\varphi_i - \text{mean}(\varphi_i)}{\text{std}(\varphi_i)}, \quad i \in [1-4] \quad (26)$$

where φ_i , $i = 1, 2, 3, 4$, represents the vessel features of φ_{sato} , φ_{frangi} , φ_{medial} , and φ_{strain} , respectively, $\hat{\varphi}_i$ ($i = 1, 2, 3, 4$) is the normalized results, and $\text{mean}(\cdot)$ and $\text{std}(\cdot)$ represent average and standard deviation, respectively. We construct a feature matrix ($N \times 4$) and input it into ELM for training and testing.

Figure 6 shows a flowchart of liver-vessel segmentation based on ELM. First, the training data is processed by four filters including the Sato, Frangi, offset medialness and strain energy filters to extract the vessel features, and a normalized operation on each feature is used to reduce the classification error. Then, the ELM learning algorithm is applied to train the SLFNs to obtain the parameters of hidden layer output matrix \mathbf{H}_E and output weights β . Finally, the ELM is utilized to recognize the liver vessels from the testing data.

Experiments

The proposed method is tested on six clinical CT data sets at portal venous phase, which were acquired on one Philips Brilliance 64 CT scanner with each slice axis plane resolution of 512×512 pixels and thickness of 0.5–2 mm. There are 100,000 samples in the training data set, and 3.87% of them are marked as liver vessels. All experiments are performed in a 64-bit Windows 7 Operating System running on a computer with an i7-4700MQ 2.4 GHz CPU, NVidia GeForce GT 740 GPU, and 16 GB RAM.

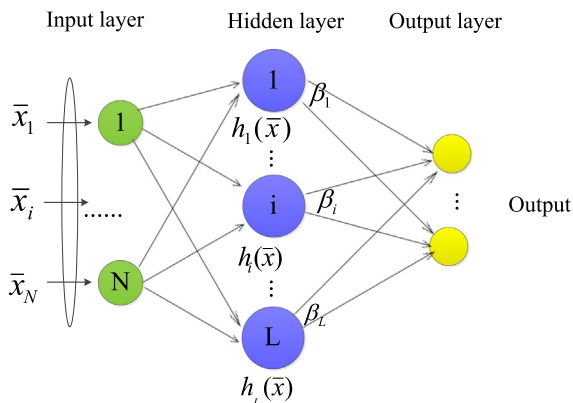


Figure 5. The network structure of SLFNs.

The hidden-node number of ELM is usually selected based on the analyses of regression or classification performance. In this paper, it is selected by balancing the training time and segmentation sensitivity (refer to Eq. (28)), a measure to quantify the segmentation performance and a higher value a better segmentation result. Figure 7 shows the effect of the hidden-node number of ELM on segmentation performance. As observed, with the increasing of the hidden-node number, the training procedure takes longer time. At the same time, the segmentation sensitivity keeps relatively stable when the hidden-node number is bigger than 50, and the corresponding training time is about 1.3 s, which is apparently less than the training time of SVM with 32 s in our experiments. Therefore, we set the hidden-node number as 50 in our paper.

Due to the lack of a suitable publicly available database, the results of the proposed method for our data set are compared with those of the geodesic active contour (GAC) [18], active contour without edge (also called CV model) [19], Conversano et al. [13], Smistad et al. [20], and the SVM-based methods. It should be mentioned that the implementations of GAC, CV model and the method in [20] are downloaded from the ITK package, MATLAB CENTRAL 3D image segmentation toolbox and tube segmentation framework software, respectively. In addition, the SVM-based method is performed using a SVM toolbox in MATLAB and shares the same training and testing data of ELM. To compare the best possible results among these methods, we manually choose vessel seeds for GAC and CV segmentation, and optimize their parameters on various CT images to maximize the vessel regions and simultaneously avoid over segmentation.

Figure 8 shows four randomly selected liver-vessel segmentation results, in which the first row gives four enhanced liver-vessel images by adjusting window width/level and the subsequent six rows show the liver-vessel segmentation results of GAC, CV model, the methods in [13,20], the SVM-based method and the proposed method, respectively. The segmentation results of the GAC, CV model and the method in [20] contain fewer thin vessels or some thick vessels compared with our method, and those of the method in [13] and the SVM-based method are close to the segmentation results of the proposed method. However, the proposed method avoids an experimental selection of segmentation parameters compared with the method in [13] and takes less training time than the SVM-based method.

To further evaluate the segmentation performance of our method, we invite a radiology expert with extensive clinical experience to establish the ground truth of liver-vessel segmentation. First, the interactive liver-vessel segmentation is performed by a trained operator using ITK-SNAP tools, which is a software application that allows users to manually delineate anatomical regions of interest. Then, the expert is asked to correct the segmentation results slice by slice. To quantify the segmentation performance, three measures including accuracy, sensitivity, and specificity are used in this paper, which can be respectively defined as:

$$\text{Accuracy} = \frac{TP + TN}{TP + FN + TN + FP} \quad (27)$$

$$\text{Sensitivity} = \frac{TP}{FP + TN} \quad (28)$$

$$\text{Specificity} = \frac{TN}{FP + TN} \quad (29)$$

where TP and TN indicate the numbers of voxels correctly classified as vessels and background and FN and FP denote the numbers of voxels improperly classified as background and vessels, respectively.

Table 1 illustrates the results of different methods on six liver CT volumes. As observed, the average segmentation accuracy and sensitivity of the proposed method are 98.1% and 74.2%, respectively,

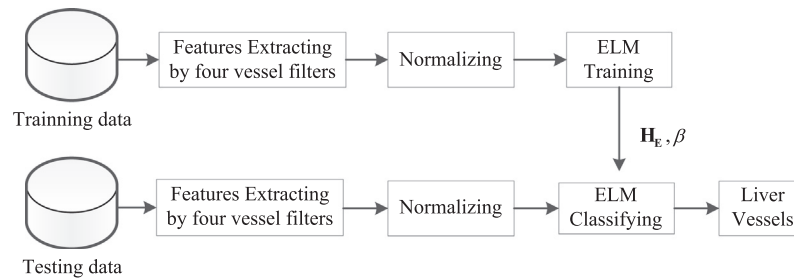


Figure 6. Flowchart of training and classifying liver vessels based on ELM.

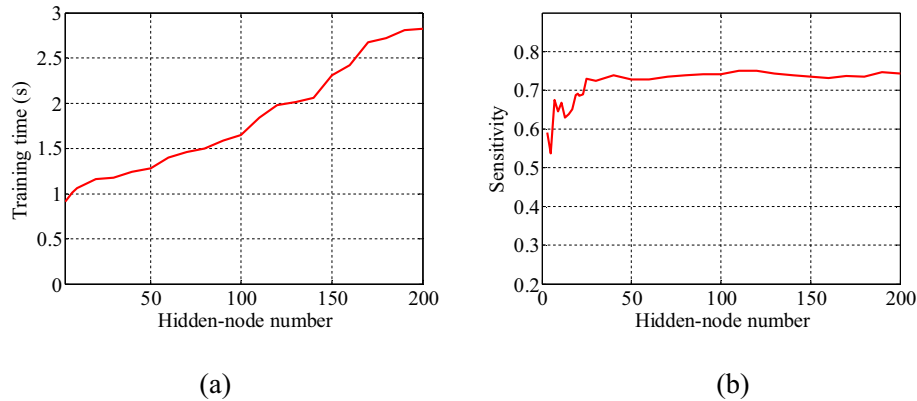


Figure 7. The effect of the hidden-node number of ELM on (a) training time and (b) segmentation sensitivity.

which are superior to those of the other methods. The average specificity of the proposed method is higher than that of CV model, the methods in [13,20] and the SVM-based method, but is slightly lower than that of the GAC method, which is mainly because the liver vessels extracted by GAC are narrower than those extracted by the proposed method, as shown in the second and last rows of Fig. 8.

Compared with the accuracy and specificity, the sensitivity of the proposed method is not very high, which is mainly because the filters used in our method cannot detect the vessel structures with low contrast, such as the portal vein, as closed by the white circle in Fig. 9, which fails to be segmented but can be found by the radiologist in terms of the anatomy knowledge and the relevance between adjacent slices. For example, the intensity of the vessels is usually higher than that of the background in the enhanced CT images, and the shape and position of the vessels usually maintain continuity between adjacent slices.

Discussion and conclusions

Due to the complexity of 3D liver vessels, few machine learning based methods are used for liver-vessel segmentation. This paper proposes a method for liver-vessel segmentation from contrast-enhanced CT Images based on ELM. First, an anisotropic filter is used to remove noise as well as preserve vessel boundaries. Then, based on the analysis of vessel shapes, three classical vessel filters including the Sato, Frangi, offset medialness filters are utilized to extract the shape features. In addition, the strain energy filters is introduced to preserve vascular structures like the bifurcations and branches. Next, a normalized operation is used to reduce the classification error caused by different intensity ranges of each vessel feature. Finally, an ELM is applied to train and classify liver vessels from background voxels.

As the processing procedure on abdomen CT volumes always suffers from heavily computation burden, several efforts have been made to improve the efficiency of the proposed method:

- (1) The implementation of liver-vessel detection and segmentation is performed only in liver regions rather than in the whole abdominal CT datasets. Therefore, it can obviously reduce the computation time as well as the dependence on high performance computers, especially on large memory and high performance CPU computers.
- (2) The ELM is applied to train and classify liver vessels from background voxels for its fast learning speed and good generalization ability. In the training procedure, we select the hidden-node number of ELM to balance the training time and segmentation sensitivity, and the training time is less than 1.5 s for 100,000 training voxels, which is obviously superior to that of SVM with 32 s. In the classifying procedure, we remove some unnecessary data to further reduce the memory usage and running time. For instance, the voxels whose filtering results equal zeroes are directly set as background region. In fact, the testing time is in a range of [0.05 s, 0.1 s] for each CT volume.

In addition, once the training procedure is finished, the proposed method does not require the manual selection of the initial vessel regions for each CT volume as the GAC and region growing methods do. Moreover, our method involves only few parameters for ELM, and these parameters can be easily confirmed in a reasonable range compared with the GAC, the region growing and the threshold-based methods. For example, the GAC method needs carefully set the propagating coefficient to avoid boundary leakage with weak vessel boundaries, and the region growing based method is sensitive to the noise and hence it is difficult to design predefined criteria grouping pixels (voxels) or sub-regions with similar properties of the seeds into larger regions. As the intensity of thick vessels is higher than that of thin and weak vessels, the threshold-based method often suffers from intensity inhomogeneity and therefore is difficult to effectively separate the vessels from the background.

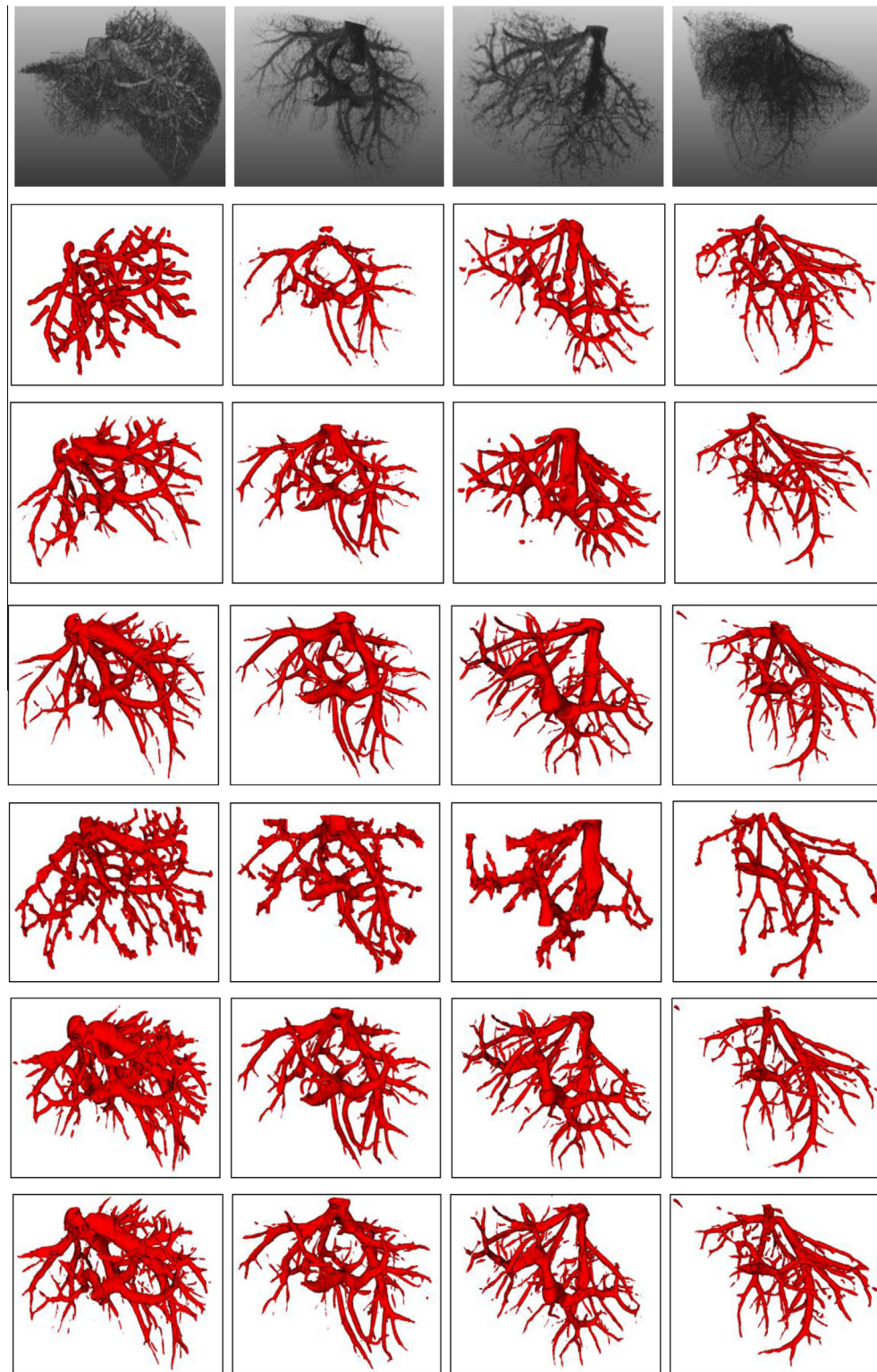


Figure 8. Liver-vessel segmentation results of different methods. The first row is the enhanced 3D liver-vessel images; the second through last rows are the results of the GAC [18], CV model [19], Conversano et al. [13], Smistad et al. [20], the SVM-based method and the proposed method, respectively. The borders in the images from the second through last rows are added for clarity.

Experimental results on medical CT data sets show that the proposed method can segment liver vessels accurately, achieving accuracy, sensitivity and specificity of 98.1%, 74.2% and 99.3%, respectively, and has a better performance on extracting thin vessels than the GAC and CV model. Furthermore, since the four filters work well for the detection of the general tubular structures,

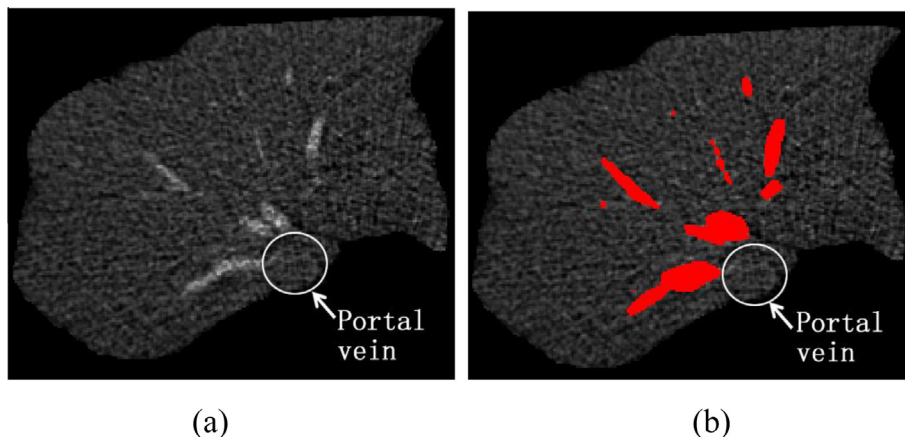
our method can be generalized for other 3D vessel extraction like cerebral vascular vessels.

Currently, our method mainly focuses on the application of machine learning method to segment 3D vessels, and there still exist some drawbacks. For example, it is sensitive to the contrast between liver vessels and parenchyma, which is also a common

Table 1

Comparison of segmentation performance of different methods.

Methods	Accuracy	Sensitivity	Specificity
GAC [18]	0.966	0.357	0.996
CV model [19]	0.977	0.713	0.990
Conversano et al. [13]	0.973	0.723	0.989
Smistad et al. [20]	0.970	0.571	0.990
SVM	0.978	0.734	0.990
Ours	0.981	0.742	0.993

**Figure 9.** Unsuccessful segmentation of portal vein due to low contrast. (a) Original liver slice and (b) segmentation result (red regions). (For interpretation of the references to colour in this figure legend, the reader is referred to the web version of this article.)

problem for the intensity- and gradient-based methods like region growing and GAC methods. In addition, our method takes more running time than GPU-based method [20] does. We will focus on increasing the robustness of the proposed method for low contrast CT volumes, and improving its efficiency for the multi-feature extraction and multi-scale operation by the GPU-based algorithms.

Acknowledgments

This work is supported by the National Natural Science Foundation of China (Grant nos. 61172184, 61379107, 61402539, and 61573380), Program for New Century Excellent Talents in University of Education Ministry in China (Grant no. NCET-13-0603), Specialized Research Fund for the Doctoral Program of Higher Education in China (Grant no. 20130162110016), Science and Technology Project of Hunan Province, China (Grant no. 2015RS4008), Program for Hunan Province Science and Technology Basic Construction (Grant no. 20131199), Fundamental Research Funds for the Central Universities of Central South University (Grant no. 2014ZZTS053), and Hunan Provincial Innovation Foundation for Postgraduate (Grant no. CX2014B052).

The authors thank the editors and anonymous reviewers for their valuable comments that greatly improved the paper's quality. We also thank Dr. Changyan Xiao, a Professor of Hunan University, Changsha, P. R. China, for his help on this work.

References

- [1] Selle D, Preim B, Schenk A, Peitgen HO. Analysis of vasculature for liver surgical planning. *IEEE Trans Med Imag* 2002;21:1344–55.
- [2] Lesage D, Angelini ED, Bloch I, Funka-Lea G. A review of 3D vessel lumen segmentation techniques: model, features and extraction schemes. *Med Image Anal* 2009;13:819–45.
- [3] Frangi AF, Niessen WJ, Vincken KL, Viergever MA. Multiscale vessel enhancement filtering. *Med Image Comput Assist Interv* 1998;1496:130–7.
- [4] Xiao C, Staring M, Wang Y, Shamonin DP, Stoel BC. Multiscale bi-Gaussian filter for adjacent curvilinear structures detection with application to vasculature images. *IEEE Trans Image Process* 2012;22:174–88.
- [5] Vasilevskiy A, Siddiqi K. Flux maximizing geometric flows. *IEEE Trans Pattern Anal Mach Intell* 2002;24:1565–78.
- [6] Law MW, Chung AC. Three dimensional curvilinear structure detection using optimally oriented flux. *ECCV* 2008;5305:368–82.
- [7] Turetken E, Becker C, Glowacki P, Benmansour F, Fua P. Detecting irregular curvilinear structures in gray scale and color imagery using multi-directional oriented flux. *ICCV* 2013:1553–60.
- [8] Lorigo LM, Faugeras OD, Grimson WEL, Keriven R, Kikinis R, et al. CURVES: curve evolution for vessel segmentation. *Med Image Anal* 2001;5:195–206.
- [9] Shang Y, Deklerck R, Nyssen E, Markova A, Mey JD, et al. A vessel active contour model for vascular segmentation. *IEEE Trans Biomed Eng* 2011;58:1023–32.
- [10] Bauer C, Pock T, Sorantin E, Bischof H, Beichel R. Segmentation of interwoven 3d tubular tree structures utilizing shape priors and graph cuts. *Med Image Anal* 2010;14:172–84.
- [11] Esneault S, Lafon C, Dillenseger JL. Liver vessels segmentation using a hybrid geometrical moments/graph cuts method. *IEEE Trans Biomed Eng* 2010;57:276–83.
- [12] Hemmatia H, Kamli-Asl A, Talebpour A, Shirani S. Semi-automatic 3D segmentation of carotid lumen in contrast-enhanced computed tomography angiography images. *Physica Medica* 2015;31(8):1098–104.
- [13] Conversano F, Franchini R, Demitri C. Hepatic vessel segmentation for 3D planning of liver surgery: experimental evaluation of a new fully automatic algorithm. *Acad Radiol* 2011;18:461–70.
- [14] Sato Y, Nakajima S, Shiraga N, Atsumi H, Koller T, Gerig G, et al. Three-dimensional multiscale line filter for segmentation and visualization of curvilinear structures in medical images. *Med Image Anal* 1998;2:143–68.
- [15] Krissian K, Malandain G, Ayache N. Model-based detection of tubular structures in 3D images. *Comput Vis Image Understanding* 2000;80:130–71.
- [16] Xiao C, Staring M, Shamonin D, Reiber JHC, Stolk J, Stoel BC. A strain energy filter for 3D vessel enhancement with application to pulmonary CT images. *Med Image Anal* 2011;15:112–24.
- [17] Huang GB, Zhu QY, Siew CK. Extreme learning machine: theory and applications. *Neurocomputing* 2006;70:489–501.
- [18] Caselles V, Kimmel P, Sapiro G. Geodesic active contours. *Int J Comput Vis* 1997;22:61–79.
- [19] Zhang Y, Matuszewski BJ, Shark LK, Moore CJ. Medical image segmentation using new hybrid level-set method. *IEEE Int Conf Bio Vis* 2008:71–6.
- [20] Smistad E, Elster AC, Lindseth F. GPU accelerated segmentation and centerline extraction. *Int J CARS* 2014;9:561–75.